JOURNAL OF GEOPHYSICAL RESEARCH, VOL. 114, C02018, doi:10.1029/2007JC004411, 2009

Flow separation and resuspension beneath shoaling nonlinear internal waves

Leon Boegman[1] and Gregory N. Ivey[2]

Received 20 June 2007; revised 25 August 2008; accepted 19 September 2008; published 24 February 2009.

[1] Laboratory observations are presented showing the structure and dynamics of the turbulent bottom boundary layer beneath nonlinear internal waves (NLIWs) of depression shoaling upon sloping topography. The adverse pressure gradient beneath the shoaling waves causes the rear face to steepen, flow separation to occur, and wave-induced near-bottom vortices to suspend bed material. The resuspension is directly attributed to the near-bed viscous stress and to near-bed patches of elevated positive Reynolds stress generated by the vortical structures. These results are consistent with published field observations of resuspension events beneath shoaling NLIWs. Elevated near-bed viscous stresses are found throughout the domain at locations that are not correlated to the resuspension events. Near-bed viscous stress is thus required for incipient sediment motion but is not necessarily a precursor for resuspension. Resuspension is dependent on the vertical velocity field associated with positive Reynolds stress and is also found to occur where the mean (wave-averaged) vertical velocity is directed away from the bed. The results are interpreted by analogy to the eddy-stress and turbulent bursting resuspension models developed for turbulent channel flows.

Citation: Boegman, L., and G. N. Ivey (2009), Flow separation and resuspension beneath shoaling nonlinear internal waves, *J. Geophys. Res.*, *114*, C02018, doi:10.1029/2007JC004411.

1. Introduction

[2] Progressive nonlinear internal waves (NLIWs) are ubiquitous features of lakes and coastal oceans [e.g., *Jackson*, 2007]. Shoreward propagating NLIWs will shoal upon sloping topography generating localized patches of energetic turbulence, mixing, nutrient flux and sediment resuspension [e.g., *Dickey et al.*, 1998; *MacIntyre et al.*, 1999; *Klymak and Moum*, 2003; *Hosegood and van Haren*, 2004; *Bogucki et al.*, 2005]. Of these processes, the dynamics of sediment resuspension resulting from NLIW shoaling remain comparatively uninvestigated.

[3] Resuspension in the benthic boundary layer (BBL) occurs when stress is applied to the bed material. The total stress τ in a steady isotropic turbulent BBL over a flat bottom is the sum of the viscous stress τ_ν and Reynolds stress τ_R components

$$\tau = \rho_o u_*^2 = \tau_\nu + \tau_R = \nu\rho_o \frac{\partial \bar{u}}{\partial z} + \rho_o \overline{u'w'}. \quad (1)$$

where ν is the kinematic viscosity and ρ_o = 1000 kg m^3 a reference density. Near the bed, within the viscous sublayer, the Reynolds stress is small and $\tau_R \ll \tau_\nu$. Because of the thinness of the viscous sublayer (O1 mm [*Caldwell and Chriss*, 1979]), the shear stress at the bed

$$\tau_o = \rho_o u_*^2|_{z=0} \quad (2)$$

is estimated from the friction velocity u_* by fitting measured $\bar{u}$ profiles within the logarithmic layer to the law of the wall

$$\frac{\bar{u}}{u_*} = \frac{1}{\kappa} ln \frac{z}{z_o} \quad (3)$$

where κ = 0.41 is the von Kármán constant and z_o the roughness length scale [e.g., *Lorke et al.*, 2002].

[4] Field-scale hydrodynamic and sediment transport models typically apply a free-slip bottom boundary condition and do not resolve the logarithmic velocity profile. In these models, τ_o is evaluated from a parameterization of u_* in terms of the resolved near-bed horizontal velocity U and a drag coefficient C_D

$$u_*^2 = C_D U^2. \quad (4)$$

[5] In barotropic flows, U results from wave orbital motions and quasi-steady tides or seiches [e.g., *Drake and Cacchione*, 1986; *Dickey et al.*, 1998; *Wiberg et al.*, 1994]. Resuspension is expected when τ_o exceeds a threshold criterion for incipient sediment motion, the critical Shields parameter (see for further discussion *Smyth and Hay* [2003]). Observations of resuspension beneath shoaling

[1]Department of Civil Engineering, Queen's University, Kingston, Ontario, Canada.
[2]School of Environmental Systems Engineering, University of Western Australia, Crawley, Western Australia, Australia.

0148-0227/09/2007JC004411$09.00

internal waves [*Klymak and Moum*, 2003; *Hosegood and van Haren*, 2004] and observations of nepheloid layers in lakes and oceans, where the topographic slope angle is critical for internal wave/tide reflection [*Hawley*, 2004; *McPhee-Shaw et al.*, 2004; *Puig et al.*, 2004], show that baroclinic processes will also lead to resuspension of benthic material and the τ_o threshold criterion has been incorporated into circulation and sediment transport models for stratified flows [e.g., *Cacchione and Drake*, 1986; *Ribbe and Holloway*, 2001; *Wang and Pinardi*, 2002; *Kuhrts et al.*, 2004].

[6] The stress-based geophysical models described above have been developed from the considerable research on sediment resuspension in turbulent channel flows. *Bagnold* [1966] conceptually decomposed the mechanisms leading to resuspension of bed material, beginning with initiation of sediment motion due to bed shear followed by entrainment of the sediment into the free-stream flow by the vertical component of the velocity field. *Sutherland* [1967] further hypothesized that turbulent eddies moving toward the boundary would create the necessary bed shear stress, thus initiating sediment motion. In this ''eddy-stress'' model, the sediment would then be susceptible to entrainment by the vertical velocity component of the eddy.

[7] Numerous laboratory [*Wei and Willmarth*, 1991; *Ikeda and Asaeda*, 1983; *Bennett and Best*, 1995] and field studies in steady unidirectional flows support these models. In a sand-bed river, for example, suspension was traced to energetic burst-like turbulent events during which upward transport of momentum and sediment are correlated [*Lapointe*, 1996]. In a tidal current, bursting events were associated with enhanced Reynolds stress and resuspension [*Soulsby et al.*, 1994]. Numerical simulations of the fluid and sediment equations for turbulent channel flow also reveal a correlation between the sediment concentration and near-bed vertical velocity [*Zelder and Street*, 2001]. Visualization of the flow suggests that coherent vortical structures within the turbulent boundary layer may be an important mechanism for vertical entrainment of sediment.

[8] The applicability of (3) and (4) to unsteady and nonstationary flows remains questionable. While these equations have been shown to capture the turbulent dynamics of high-speed oscillatory tidal flows [*Stacey et al.*, 1999], low-velocity seiche currents in lakes exhibit near-bottom current profiles and dissipation rates that are inconsistent with steady state law of the wall scaling and associated estimates of both u_* and z_o [*Lorke et al.*, 2002]. It is thus not expected that models based on (3) and (4) will be able to capture resuspension associated with shoaling NLIWs. Nonetheless, remarkable analogies to the eddy-stress resuspension model may be found in wavy flows.

[9] *Thorpe* [1998] proposed that a shoaling internal wave would form a rotor beneath the wave as it breaks, with flow contrary to the forward overturning of surface waves on a beach (the terms rotor, eddy and vortex are used interchangeably in this manuscript). A rotor has indeed been observed beneath shoaling NLIWs [*Hosegood and van Haren*, 2004], where strong vertical velocities at the leading edge correlate to massively enhanced sediment fluxes. Large τ_o was also observed at other times, but with no enhanced flux.

[10] NLIW induced resuspension is also expected in the absence of shoaling bathymetry. Direct numerical simulations of large-amplitude NLIWs of depression propagating over flat topography develop a jet flow beneath the wave trough because of the proximity of the bottom boundary. The resulting adverse pressure gradient at the trailing edge of the wave leads to flow separation, elevated levels of τ_o and the periodic shedding of coherent vortex structures that ascend high into the water column [*Hammond and Redekopp*, 1998; *Stastna and Lamb*, 2002; *Diamessis and Redekopp*, 2006]. This ''global instability'' mechanism is believed to favor resuspension; however, validation of this hypothesis against field data remains difficult, e.g., during the passage of NLIWs, peaks in the vertical flux of suspended material have been correlated with both local minima [*Bogucki et al.*, 1997] and local maxima [*Dickey et al.*, 1998; *Bogucki et al.*, 2005] in τ_o. Laboratory experiments [*Carr and Davies*, 2006] reproduce the jet flow as well as revealing short intervals in which relatively strong vertical motions are observed in the vicinity of the expected separation bubble.

[11] In the present study, laboratory experiments are analyzed to reveal the transient spatial structure of the resuspension, velocity and stress fields as NLIWs shoal upon sloping topography. These observations will allow detailed investigation of the sediment resuspension mechanism beneath shoaling NLIWs. The waves are incident upon shoaling topography in the form of a closed slope, as opposed to slope-shelf topography or a topographic ridge. Closed slope topography is characteristic to most lakes and many coastal oceans at the depth of NLIW shoaling, e.g., Mono Lake [*MacIntyre et al.*, 1999], Lake Biwa [*Boegman et al.*, 2003], Lake Michigan [*Hawley*, 2004], the Oregon continental shelf [*Klymak and Moum*, 2003], the Alboran slope [*Puig et al.*, 2004], the Australian north west shelf [*Ribbe and Holloway*, 2001], and the Faeroe-Shetland Channel [*Hosegood and van Haren*, 2004].

[12] The majority of previous studies on shoaling NLIWs were concerned with slope-shelf topography. For example, the laboratory work by *Helfrich and Melville* [1986] and *Kao et al.* [1985] considered two-layer systems where instability and localized mixing were observed in the neighborhood of the shelf break. Similar numerical investigations on slope-shelf topography have addressed the dynamics and location of wave breaking and the formation of waves with trapped cores [e.g., *Vlasenko and Hutter*, 2002; *Lamb*, 2003; *Venayagamoorthy and Fringer*, 2007]. NLIW transmission over a submerged topographic ridge and the associated breaking condition has also been experimentally analyzed [*Wessels and Hutter*, 1996; *Sveen et al.*, 2002].

[13] Several laboratory studies have examined the shoaling of NLIWs upon closed slopes in a two-layer fluid. *Wallace and Wilkinson* [1988] found breaking of periodic incident waves to be initiated by the interaction of the incident wave with the return flow of the preceding wave. For lone NLIWs, *Helfrich* [1992] and *Michallet and Ivey* [1999] computed that between 5% and 25% of the incident nonlinear wave energy may be converted by diapycnal mixing to an irreversible increase in the potential energy of the water column. *Boegman et al.* [2005b] considered the degeneration of a basin-scale internal wave into an NLIW

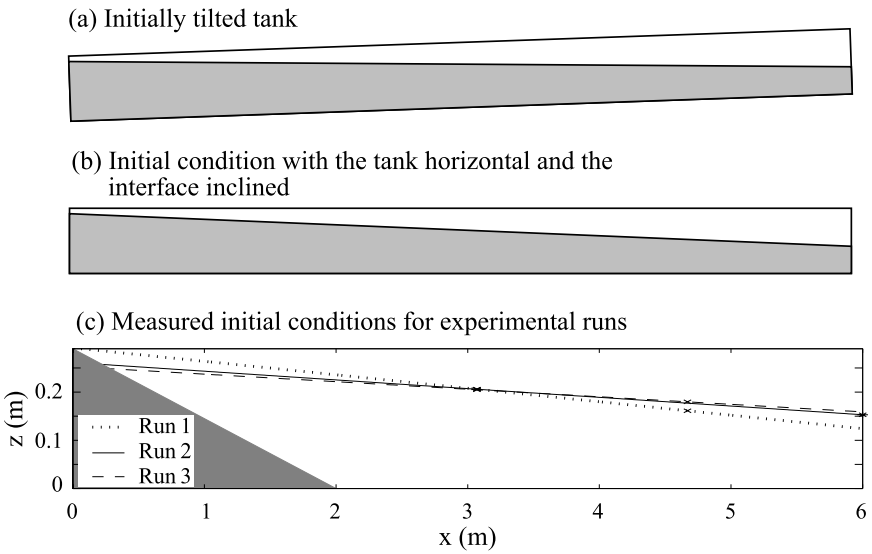

Figure 1. Schematic diagram of the experimental setup and forcing mechanism. (a) Initially tilted tank. (b) Initial condition with the tank horizontal and the interface inclined. (c) Schematic diagram of the experimental facility showing initial condition at $t = 0$ with upwelling at the slope. Initial condition is a linear fit to electronic measurements from ultrasonic wave gauges (multiplication signs) and manual measurements using a ruler (asterisks). Wave gauge locations are as follows: wave gauge A at $x = 3.07$ m and wave gauge B at $x = 4.67$ m.

packet and modeled both the reflection coefficient and the breaker type. While much has been learned about shoaling of NLIWs, these studies were not concerned with sediment resuspension, the focus of the present paper.

[14] The remaining sections of the manuscript are organized as follows. In 2 and 3, we describe the experimental methods and present the results, respectively. In 4, the results are interpreted by analogy to present resuspension models and breaking criteria. The applicability of the results to a generalized geophysical context is also discussed, followed by concluding remarks in 5.

2. Experimental Methods

[15] The experiments were conducted in a sealed rectangular acrylic tank (600 cm long, 29 cm deep, and 30 cm wide) into which a uniform slope of 0.145 was inserted, extending the entire height of the tank and positioned at one end (Figure 1c). The tank was filled with an approximate "two-layer" stratification consisting of a hyperbolic tangent density profile with a thinner upper fluid layer that supports NLIWs of depression [see *Horn et al.*, 2001; *Boegman et al.*, 2005a, 2005b]. The density difference between the upper and lower layers $\rho_2 - \rho_1 \approx 20\ \mathrm{kg\ m^{-3}}$ ($\pm 2\ \mathrm{kg\ m^{-3}}$) giving a linear long wave speed $c_o = \sqrt{g' h_1 h_2 / H} \approx 0.11\ \mathrm{m\ s^{-2}}$, where the tank depth $H = h_1 + h_2 = 0.29$ m and the reduced gravity at the interface $g' = g(\rho_2 - \rho_1)/\rho_2 \approx 0.20\ \mathrm{N\ kg^{-1}}$. The period of the gravest mode internal seiche (horizontal mode one) is $T_i = 2L/c_o \approx 100$ s, where L is the tank length.

[16] With a lake application in mind, the tank was rotated to the required interfacial displacement angle prior to commencing an experiment (Figure 1a). From this condition, the setup and subsequent relaxation from a wind stress event was simulated through a rapid rotation of the tank to the horizontal position, leaving the interface inclined at the original angle of tilt of the tank (Figure 1b). Depending on the initial direction of rotation prior to commencing an experiment, the resulting inclined interface at time $t = 0$ could be characterized as either upwelling on the slope (Figure 1c) or downwelling along the slope, relative to the undisturbed condition. The initial conditions for this set of experiments composed of an inclined density interface and a quiescent density profile as given in Figures 1 and 2, respectively.

[17] The two-dimensional velocity field was measured using particle image velocimetry (PIV). The fluid was locally seeded with pliolite particles (106–150 μm diameter) and illuminated by a light sheet projected through the upper surface of the tank. The light sheet was generated by a linear arrangement of 12 V 50 W halogen lamps (General Electric EXT) focused to a width of 0.5 cm by a series of narrow slits. Ten-bit digital images were acquired from a 20 $\times$ 20 cm field of view using a progressive scan CCD camera at a resolution of 992 $\times$ 992 pixels (PULNiX TM-1040 camera, Navitar ST16160 lens). The individual frames were captured at 30 Hz with no shutter in a LabVIEW environment using a digital framegrabber (National Instruments PCI-1422) and written in real time to disk (VisionStream 100 library).

[18] The vector fields were calculated at 30 Hz from particle image pairs using the MatPIV toolbox [*Sveen*, 2004]. The constant 1/30 s time interval between consecutive frames allowed the second frame of a preceding image pair to be used as the first frame of the subsequent pair. The PIV algorithm employed an adaptive multipass procedure where an interrogation window with a 50% overlap was iteratively reduced from two passes at 64 $\times$ 64 pixels to two passes at 32 $\times$ 32 pixels. The resultant velocity estimate was thus calculated at a resolution of 3.5 $\times$ 3.5 mm. Spurious vectors were removed after each pass using a local median filter. After processing, the vector field was validated with a signal-to-noise ratio filter. The final velocity

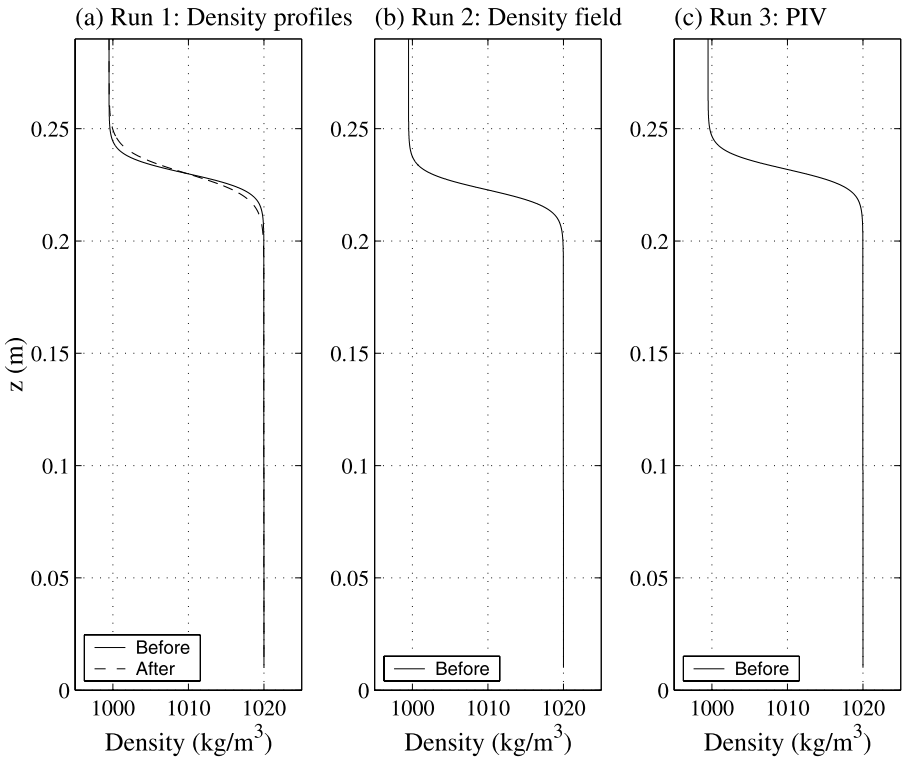

Figure 2. Measurements of the vertical density structure with the fluid quiescent both before and after the forcing event. (a) Run 1 (29-point calibration of measured profile using third-order polynomial), (b) Run 2 (two-point linear calibration of measured profile), and (c) Run 3 (two-point linear calibration of measured profile).

field was smoothed by averaging across a five frame moving window, thus removing temporal fluctuations occurring over timescales less than 0.167 s. This procedure will effectively remove experimental noise, but not turbulent fluctuations as a temporal resolution of 0.1 s has been shown to capture the turbulent characteristics of a jet flow by *Webster et al.* [2001] at Reynolds number 3000; much higher than those achieved in the present study.

[19] To visualize the flow field, digital images of the entire tank were acquired using a Canon MV-X2i digital video camera. The detailed interaction of the internal wave field with the sloping topography was also visualized using the PULNiX camera with a resolution of 1 pixel per mm at a framing rate of 5 Hz. The data collection methods, apparatus and image processing are summarized by *Boegman et al.* [2005b]. The index of refraction between the two fluid layers was not matched causing a shadowing of the density interface. This prevented quantitative mixing analysis from the images.

[20] The vertical displacements of the density interface were measured using two ultrasonic wave gauges distributed longitudinally along the tank at locations A and B (Figure 1). The wave gauges logged data to a personal computer at 10 Hz through a 16-bit analog-to-digital converter (National Instruments PCI-MIO-16XE-50). A typical time series of interfacial displacement is shown in Figure 3.

[21] The density structure was measured by vertically traversing a Fast Conductivity and Temperature Sensor (Precision Measurement Engineering) through the fluid. The direct and gradient resistances were converted to output voltages in a conditioning box, then digitized using the 16-bit analog-to-digital converter and logged to a personal computer. The voltages were converted to density by calibration against an Anton-Paar densimeter (DMA60). Measurements were made with the fluid quiescent both before and after the forcing event and this enabled the computation of the increase in potential energy of the system. Profiles were obtained in pairs to ensure that the fluid was indeed quiescent.

[22] The experimental variables considered in this study, together with the resolution with which they were determined, are given in Table 1. Previous work has measured the density field over a range of experimental variables. Because of the small field of view from the CCD camera and the impossibility of knowing *a priori* where the NLIWs would shoal as they were carried upon the internal seiche (described below), the experimental parameters associated with the PIV experiments were not varied in a systematic manner over a range of values. The wave-breaking dynamics shown herein are typical results captured during several weeks of experimentation. A comprehensive numerical study of the velocity field associated with NLIW shoaling over a range of variables is presently being undertaken and more laboratory work is planned.

3. Experimental Results

3.1. Flow Field

[23] The flow field observed in the experimental facility has been described by *Horn et al.* [2001] and *Boegman et al.*, 2005a [2005b], who considered upwelling and

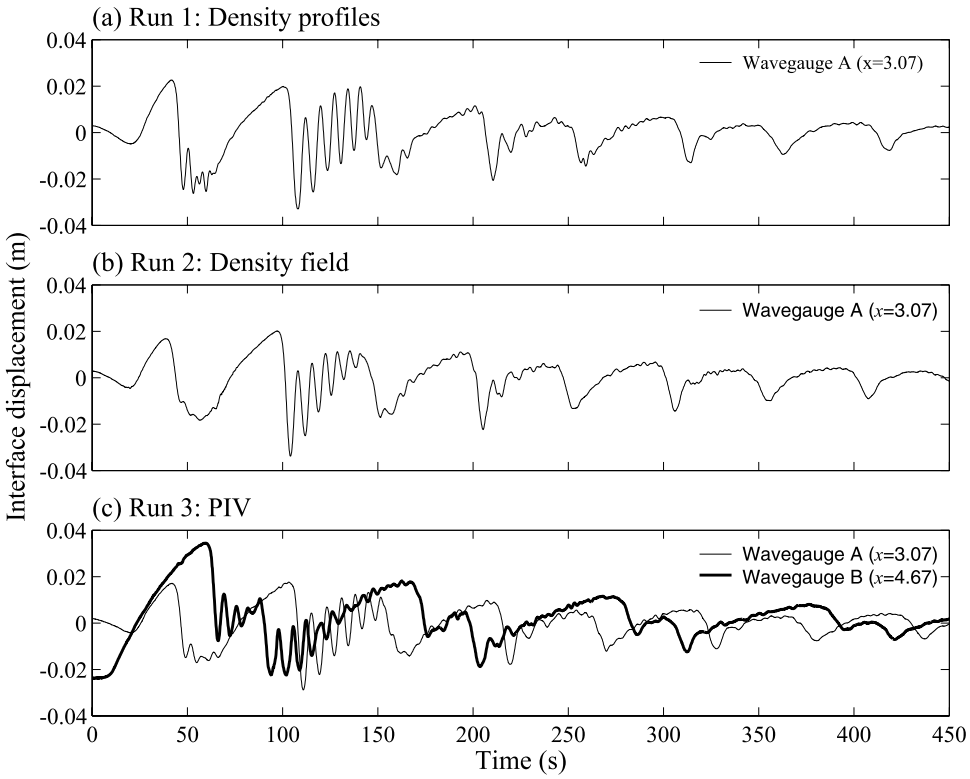

Figure 3. Time series of the observed interface displacement showing (a) Run 1, (b) Run 2, and (c) Run 3. Details of the experimental conditions are given in Table 1.

downwelling initial conditions for domains withboth vertical and sloping end walls, but did not measure fluid velocity. A typical experiment from the present set is shown in Figure 4. From the initial upwelling condition, (Figures 1 and 4a), the flow was accelerated from rest by the baroclinic pressure gradient introduced by the tilted density interface. From this initial condition, linear theory predicts that more than 98% of the available potential energy introduced by the interfacial displacement at time zero will be transferred to a horizontal mode one internal standing wave [*Boegman et al.*, 2005a]. Nonlinear steepening of the standing wave components and subsequent dispersion leads to the formation of a progressive internal surge and NLIW packet; containing as much as 20% of the initial available potential energy [*Boegman et al.*, 2005b]. Progressing initially from left to right (Figure 4b), the surge and NLIW packet are evident on wave gauge A at $t \approx 50$ s (Figure 3). Upon reflecting from the vertical end wall, the waves traveled toward the slope (100 s < t < 150 s, wave gauge A and Figure 4c) and eventually shoaled, where wave breaking was observed (Figure 4d). Not all of the wave energy was dissipated through breaking and a long wave of lower frequency was reflected ($t \approx 150$ s, wave gauge A and Figure 4e). The long wave reflected once again from the vertical wall steepening as it traveled (Figure 4f). A secondary incident wave packet (200 s < t < 250 s, wave gauge A) was observed to shoal, leading to a less energetic wave-breaking event (Figure 4g). A long wave was reflected from the secondary breaking event ($t \approx 250$ s, wave gauge A and Figure 4h). After the secondary breaking event, the remainder of the internal wave field was relatively quiescent. The wave-breaking events caused a thickening of the density interface, as wave energy was converted by diapycnal mixing to an irreversible increase in the potential energy of the water column (Figure 2a).

Table 1. Summary of Experimental Runs[a]

Run	Measurement	Initial Condition at Slope	h_1/H	η_o/h_1
1	Density profiles	Upwelling	0.3	0.96
2	Density field	Upwelling	0.3	0.62
3	Particle image velocimetry	Upwelling	0.3	0.54
4	Video frames shown in Figure 4	Upwelling	0.3	0.90

[a]The experimental variables together with the resolution with which they were determined are the tank depth $H = h_1 + h_2 = 0.29$ m, the interface depth h_1 (±0.2 cm), and the maximum excursion of the interface along the vertical end wall η_o (±0.2 cm) at time $t = 0$.

3.2. Wave Breaking, Separation, and Resuspension

[24] A sequence of images were used to examine the shoaling behavior of the primary wave packet upon the slope. In Figure 5, the panels are false color images of the density field within a rectangular subregion on the slope from Figure 4. Figure 6 shows the raw particle images and processed PIV velocity vectors corresponding to the square subregions shown in Figure 5. The velocity fields in Figure 6 were used to calculate the associated streamlines and vorticity fields (Figure 7).

[25] The first images are at $t \approx T_i$ (Table 1) and show the horizontal mode-one baroclinic seiche cresting above the slope (Figures 5a and 5b), with the corresponding weak baroclinic velocity field given in Figures 6a, 6b, 6c, and 6d. The streamlines are horizontal (Figure 7), with the exception of near the slope where there is evidence of a thin turbulent BBL. Soon thereafter, the NLIWs shoal upon the

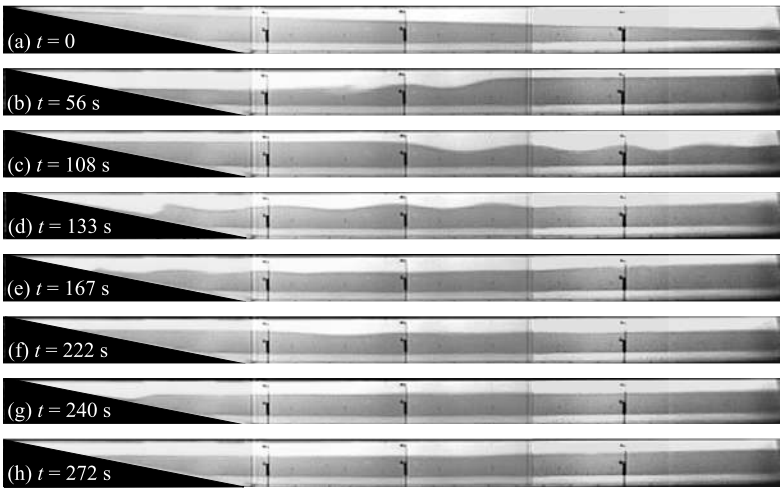

Figure 4. Video frames showing the wave field evolution for Run 4. (a) The initial condition. A surge and NLIW packets are propagating (b, c, f) to the right, (d, e, g) to the left, and (h) to the right. Wave breaking is shown to occur upon the slope. The apparent dye-free layer near the tank bottom is a spurious artifact of light reflection.

slope traveling from right to left in the upslope direction (Figures 5c, 6e, 6f, 7e, and 7f). The leading wave of depression causes a drawdown of the density interface (Figures 6c and 6d), the upslope lower-layer fluid passes beneath the wave trough (Figures 5c, 5d, 6e, 6f, 6g, and 6h) and this generates large downslope velocities in the entire lower layer (Figures 5d, 6g, and 6h). The shear across the density interface is not sufficient to cause shear instabilities, although these have been observed in other experimental runs [*Boegman et al.*, 2005b]. As the wave progresses up the slope, the rear face of the wave of depression steepens and rises into the steep front face of an incident wave of elevation (Figures 6i, 6j, 5e, 7i, and 7j). An ensuing near-bed upslope jet flow causes the downslope flow to separate;

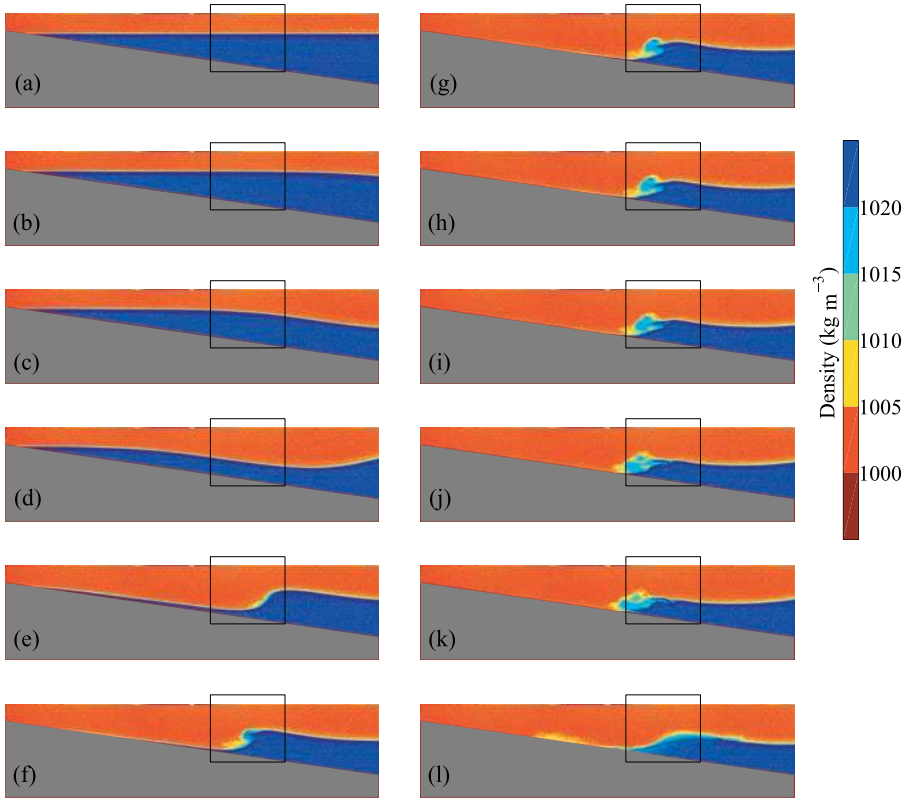

Figure 5. False color images of measured density fields from Run 2. Velocity vectors were calculated in rectangular subregion in Run 3 (Figure 6).

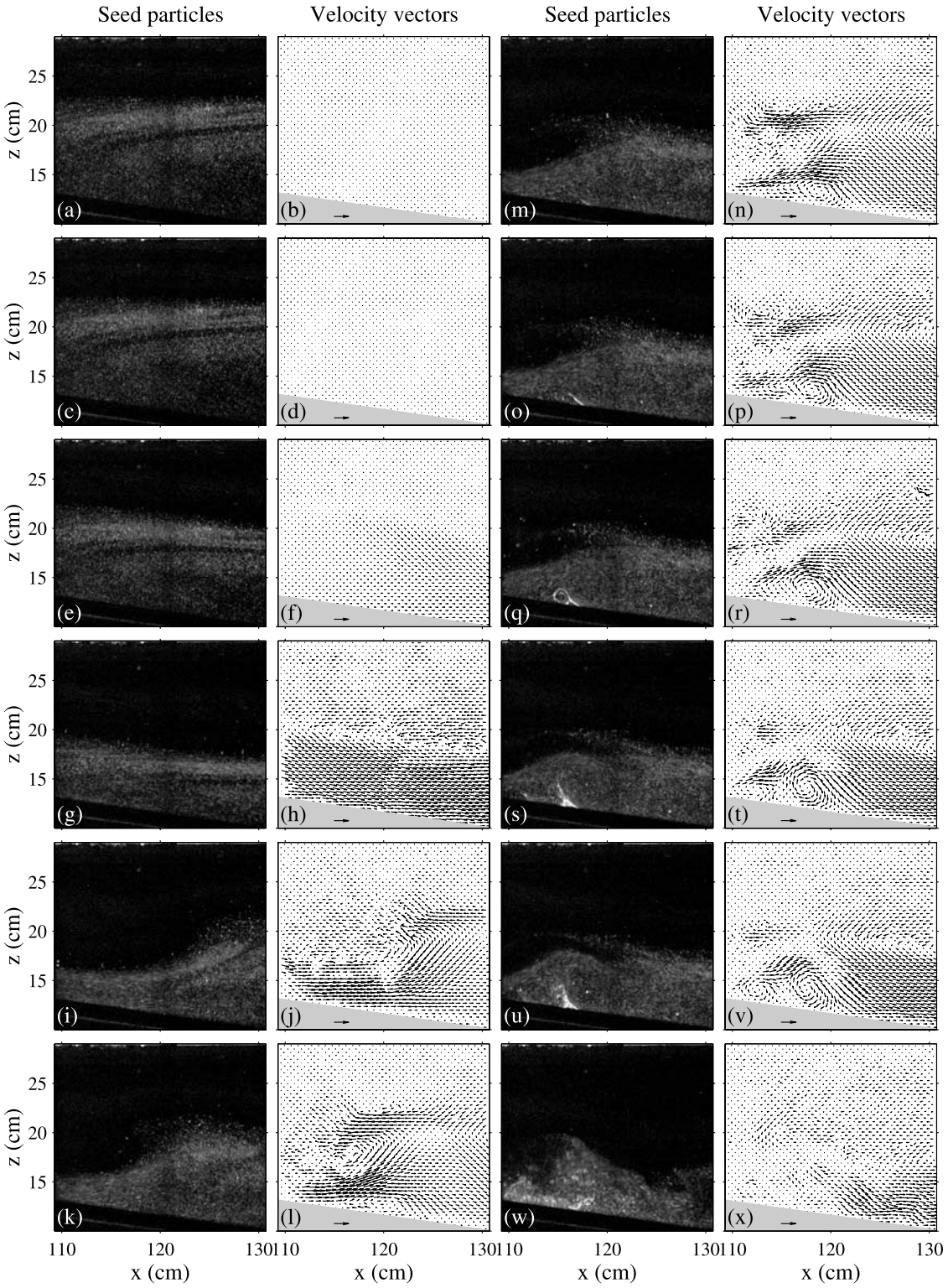

Figure 6. (a, b, c, d, e, f, g, h, i, j, k, l, m, n, o, p, q, r, s, t, u, v, w, x) Measured seed particle and velocity vector fields from Run 3. Figures 6a, 6c, 6e, 6g, 6i, 6k, 6m, 6o, 6q, 6s, 6u, and 6w show raw images of the seed particles. Figures 6b, 6d, 6f, 6h, 6j, 6l, 6n, 6p, 6r, 6t, 6v, and 6x show the velocity vector field computed from the images in Figures 6a, 6c, 6e, 6g, 6i, 6k, 6m, 6o, 6q, 6s, 6u, and 6x. Horizontal velocities are considered positive in the upslope direction. The arrow shown on the slope denotes $c_o \approx 0.11$ m s^{-1}. This data was used to compute streamlines and vorticity fields in Figure 7.

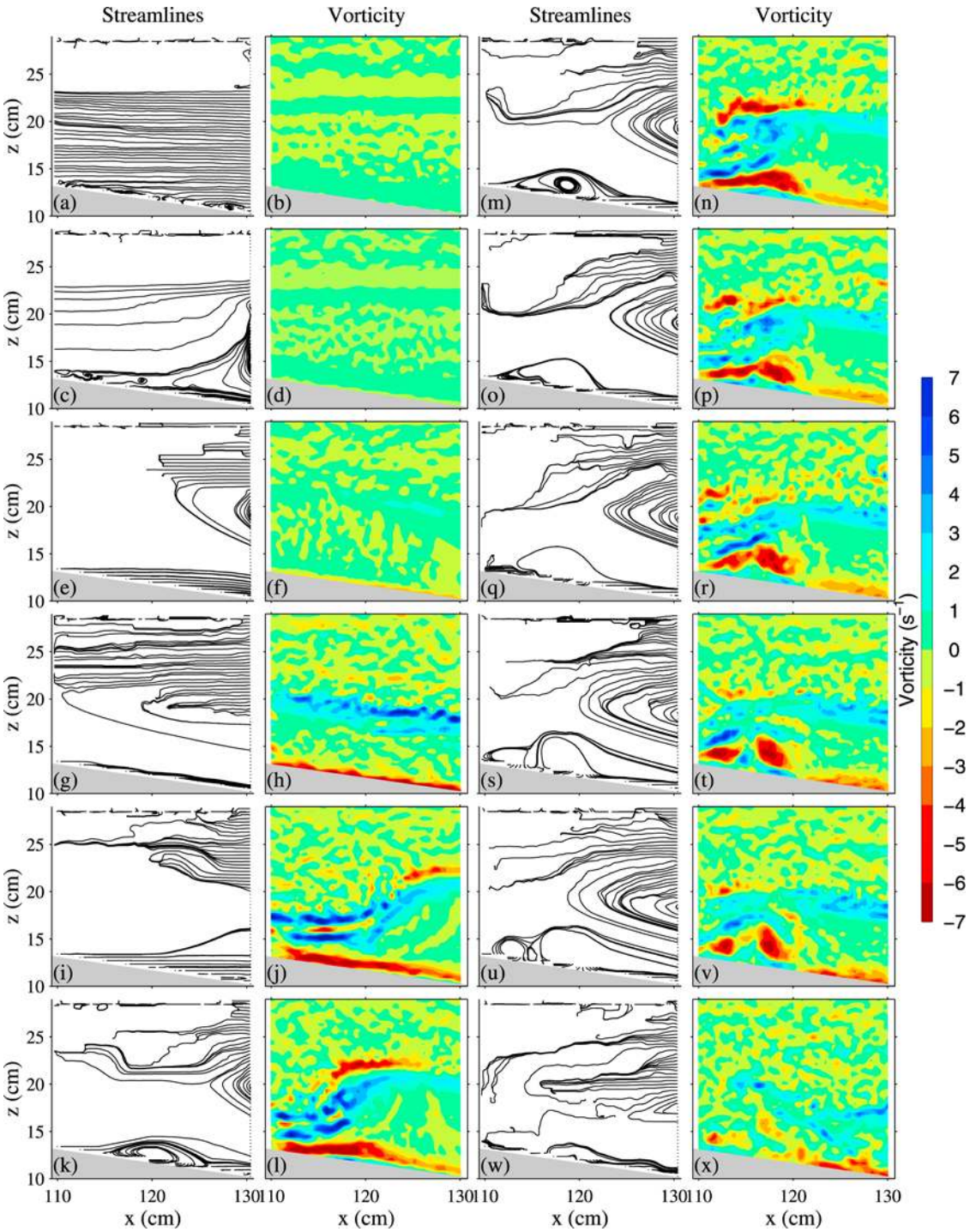

Figure 7. (a, b, c, d, e, f, g, h, i, j, k, l, m, n, o, p, q, r, s, t, u, v, w, x) Calculated streamlines (Figures 7a, 7c, 7e, 7g, 7i, 7k, 7m, 7o, 7q, 7s, 7u, and 7w) and vorticity fields (Figures 7b, 7d, 7f, 7h, 7j, 7l, 7n, 7p, 7r, 7t, 7v, and 7x) from Run 3.

observed as both positive and negative vorticity generated at the no-slip bottom boundary (Figures 6i, 6j, 6k, 6l, 7i, 7j, 7k, and 7l). The positive vorticity is generated from the upslope jet flow along the bottom boundary (120 cm < x < 130 cm) and the negative vorticity results from the downslope flow beneath the shoaling wave. A large separation bubble occurs within the adverse pressure gradient beneath the shoaling wave (Figures 7i and 7j).

[26] The velocity of the wave crest increases (Figures 6k and 6l) and the wave plunges forward becoming gravitationally unstable (Figure 5f). As this occurs, the patch of positive vorticity increases in size and strength, leading to separation of the entire downslope flow within the lower layer (at $x \approx 117$ cm) and the development of a clockwise vortex (at $x \approx 120$ cm) beneath the wave crest (Figures 5g, 6m, 6n, 7m, and 7n). The vortex, in turn, lifts high

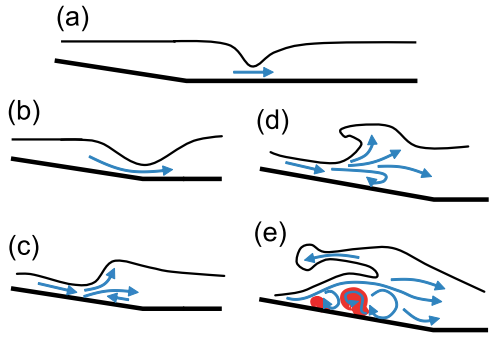

Figure 8. Schematic showing the basic elements of the internal wave-induced separation and resuspension process. (a) Offshore propagation, (b) drawdown of leading face, (c) steepening of rear face and flow separation, (d) formation of spanwise vortex, and (e) vortex-induced resuspension. Only lower-layer velocities are indicated. Shaded region denotes zones of resuspension.

concentrations of seed particles, which had been allowed to settle to the surface of the slope at the end of the previous experimental run (Figures 5g, 5h, 5i, 5j, 5k, 6m, 6n, 6o, 6p, 6q, 6r, 6s, 6t, 6u, and 6v). The newly resuspended particles are transported in a counterclockwise vortex (Figures 5i, 6q, and 6r), which interacts with the separated downslope flow, thus establishing a triplet arrangement of counter rotating vortices (Figures 6s, 6t, 6u, 6v, 7s, 7t, 7u, and 7v). These vortices are not evident in the density field (Figures 5j and 5k) indicating that entrainment of upper layer fluid into the lower layer is not occurring. Resuspension was also observed to be associated with the second weaker clockwise vortex at x = 112 cm. This cloud of suspended material is similar in form to that observed to result from turbulent ejections in a tidal flow [*Soulsby et al.*, 1994]. Eventually, the plunging wave degenerates into three-dimensional turbulence and passes from the field of view (Figures 5l, 6w, 6x, 7w, and 7x). Weak mixing of the stratifying fluid layers results. The turbulence appears to be predominantly contained within the lower layer where particles are mixed throughout the entire layer. The basic elements of this wave-induced separation and resuspension process are shown in Figure 8.

[27] The vortices beneath the breaking wave are observed to have diameters $0.2h_2^{loc} < d_v < 0.5h_2^{loc}$, where h_2^{loc} is the local lower-layer depth, and lifespans of $5 < tc_o/a < 8$, where a is the magnitude of the offshore NLIW amplitude. Despite differences in scale and topography, these values agree well with observations by others [*Sveen et al.*, 2002; *Hosegood and van Haren*, 2004].

[28] The present experiments differ from previous work on shoaling NLIWs in that the local depth on the slope is being modified by the excursion or swashing of the interface due to the internal seiche motion. In the present experiments the strong downslope flow that separates, observed beneath the shoaling NLIW prior to breaking, may be a result of the horizontal mode-one seiche phase passing from crest to trough and/or the drawdown associated with the shoaling NLIW. However, the latter effect is likely the controlling mechanism, both laboratory experiments [*Michallet and Ivey*, 1999, Figure 4] and numerical simulations [*Winters et al.*, 2000, Figure 14] show a strong downslope flow within the lower layer for the case of shoaling NLIWs of depression in a quiescent ambient flow (i.e., no horizontal mode-one seiche).

3.3. Viscous and Reynolds Stresses

[29] We investigate the relationship between stress and resuspension and assess the ability of (3) and (4) to model resuspension by calculating the spatial and temporal distributions of the two-dimensional τ_v and τ_R components of (1). As is typical for wavy and other periodic flows, the velocity field is decomposed into three components: mean $(\bar{u},\bar{w})$ (i.e., average over time), periodic $(\tilde{u},\tilde{w})$ (e.g., wave-coherent), and random local turbulent (u',w') components [*Reynolds and Hussain*, 1972; *Cantwell and Coles*, 1983; *Veron et al.*, 2007] given by

$$(u, w) = (\bar{u}, \bar{w}) + (\tilde{u}, \tilde{w}) + (u', w') \tag{5}$$

[30] The periodic components are defined as the difference $(\tilde{u}, \tilde{w}) = (u, w) - (\bar{u}, \bar{w})$ and by definition their time averages $(\bar{\tilde{u}},\bar{\tilde{w}}) = 0$. By observation, $(u',w') = 0$ during the resuspension events because resuspension is shown above to occur as a result of the wave-coherent vortices $(\tilde{u}, \tilde{w})$ generated during the early stages of NLIW shoaling prior to the observation of small-scale random three-dimensional turbulence. The wave-coherent vortices are the energy containing eddies that subsequently supply the smaller-scale turbulence that is generated as the wave breaks after the resuspension events (Figures 6w and 6x).

[31] The $\bar{u}$ field (by convention u is positive in the upslope direction) is dominated by the baroclinic flow associated with the basin-scale seiche (Figure 9a). The $\bar{w}$ velocities (Figure 9b) are associated with the transient vortices that form beneath the breaking wave and are an order of magnitude smaller than $\bar{u}$. Negative (downward) $\bar{w}$ occurs over 120 cm $< x <$ 130 cm and both negative and positive $\bar{w}$ over 110 cm $< x <$ 120 cm. Because there is not a "free-stream" vertical velocity component, the $\bar{w}$ field is entirely due to the strong vertical velocities associated with the vortices being averaged over the breaking timescale and the regions of $\bar{w} > 0$ near the bed correspond exactly to the locations of resuspension (Figures 6s and 6t). Positive vertical velocities, and the resulting weak sediment overpressure are the dominant wave-averaged process contributing to lift bed material.

[32] The nondimensional viscous stress $\tau_v = (\nu/c_o^2)\,\partial\bar{u}/\partial z$ (Figure 9c) is maximal and relatively constant through the viscous sublayer along the slope, which is $\approx$1 mm thick. A secondary weaker peak in τ_v results from the baroclinic shear across the layer interface. A boundary layer is not evident along the rigid lid of the tank where both the horizontal velocity and seed particle density (hence ability to measure velocities) are low.

[33] The nondimensional wave-averaged Reynolds shearing stress $\overline{\tau_R} = \overline{\tilde{u}\tilde{w}}/c_o^2$ (Figure 9d) is positive in the regions of resuspension, where the vortical motions are leading to ejection of both fluid and sediment from the bed ($\tilde{u} > 0$, $\tilde{w} > 0$), and negative where the largest vortex is impinging on the top of the viscous sublayer in a sweeping motion ($\tilde{u} > 0$, $\tilde{w} < 0$). Positive $\overline{\tau_R}$ is twice as large as negative $\overline{\tau_R}$. The $\overline{\tau_R}$ approaches zero within the viscous sublayer and is maximal

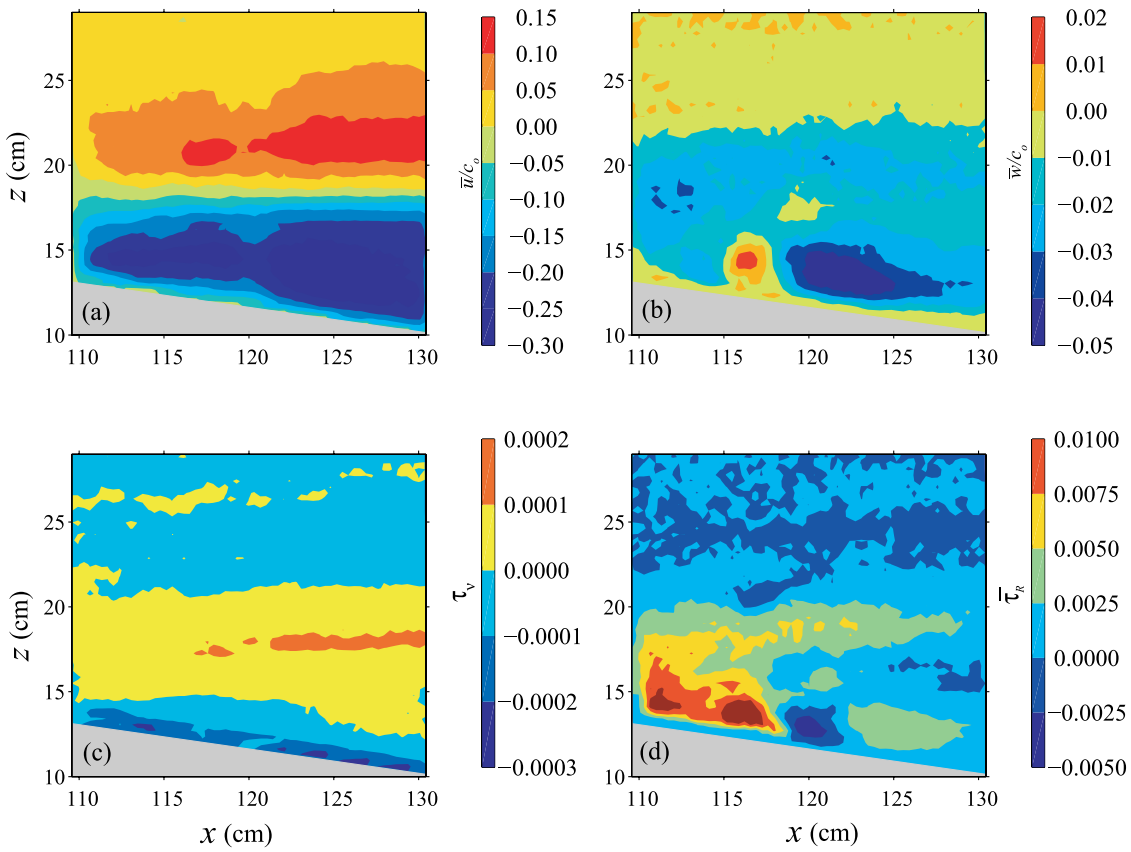

Figure 9. Nondimensional (a) mean horizontal velocity $\bar{u}/c_o$, (b) mean vertical velocity $\bar{w}/c_o$, (c) mean viscous stress $\tau_v = (\nu/c_o^2)\,\partial\bar{u}/\partial z$, and (d) mean Reynolds shearing stress $\overline{\tau_R} = \overline{\tilde{u}\tilde{w}}/c_o^2$. Horizontal velocities are positive to the left (i.e., the upslope direction).

within the wave boundary above the viscous sublayer layer, before decreasing through the upper layer. These observations qualitatively suggest that the wave-averaged dynamics are similar to the law of the wall flows in fully developed turbulent channel flows. Because $\overline{\tau_R} \to 0$ within the viscous sublayer, τ_v is still required (despite its small magnitude) to initiate sediment movement (as would be modeled by a critical Shields parameter) and make particles *available* to be lifted by the τ_R, which is an order of magnitude larger than τ_v. This observation reveals the importance of the temporal and spatial distributions of the τ_R field in lifting sediment relative to the viscous stress, which initiates movement.

[34] The instantaneous Reynolds stress $\tau_R = \tilde{u}\tilde{w}/c_o^2$ and turbulent kinetic energy TKE = $(\tilde{u}^2 + \tilde{w}^2)/c_o^2$ were computed temporally and spatially as the NLIW shoals (e.g., Figures 10 and 11). It has been suggested that both TKE and τ_R may be correlated with wave shoaling/resuspension events in the surf zone [*Foster et al.*, 2006; *Kularatne and Pattiaratchi*, 2008]. Here we consider two instantaneous observations of τ_R and TKE showing how they are highly variable in both space and time as the wave shoals.

[35] We first consider the observed period of resuspension (Figures 5k, 6u, 6v, 7u, and 7v), and second the early stage of wave shoaling where the upslope fluid is being drawndown beneath the wave trough (Figures 5e, 6i, 6j, 7i, and 7j). During resuspension, the lifted sediment associated with the large clockwise vortex at x = 118 cm and smaller clockwise vortex at x = 112 cm is correlated with positive τ_R near the bed and negative τ_R adjacent to the resuspension, where the sweeping motion transports momentum toward the bed (Figures 10a and 10b).

[36] These observations alone suggest that TKE may be a good indicator of the occurrence of resuspension process. However, during the earlier stages of shoaling, elevated levels of TKE also occur within the drawdown beneath the wave trough (Figure 11a); $\tau_R \approx 0$ at this location (Figure 11b), but is higher (both positive and negative components) near the plunging wave crest.

[37] The positive and negative τ_R components leading to resuspension in Figure 10b are due to ($\tilde{u} > 0$, $\tilde{w} > 0$) and ($\tilde{u} > 0$, $\tilde{w} < 0$), respectively (Figures 10c and 10d). Conversely, the elevated TKE during the drawdown phase results from $\tilde{u} \ll 0$ and $\tilde{w} \approx 0$ (Figures 11c and 11d); where the small $\tilde{w}$ causes $\tau_R \to 0$. This unidirectional shear flow, with high TKE but without a coherent vortex structure and associated vertical velocity and Reynolds stress, may initiate sediment movement, but is unable to lift bed material into suspension.

[38] The coincidence of the near-bed distributions of $\tilde{w} > 0$ with resuspension events and $\bar{w} > 0$ demonstrates that resuspension occurs where patches of elevated vertical velocity predominate during a shoaling event, thus providing sufficient lift (both magnitude and duration) to suspend the bed material within the complex ambient flow dynamics. On the basis of these results, it is not sufficient to model

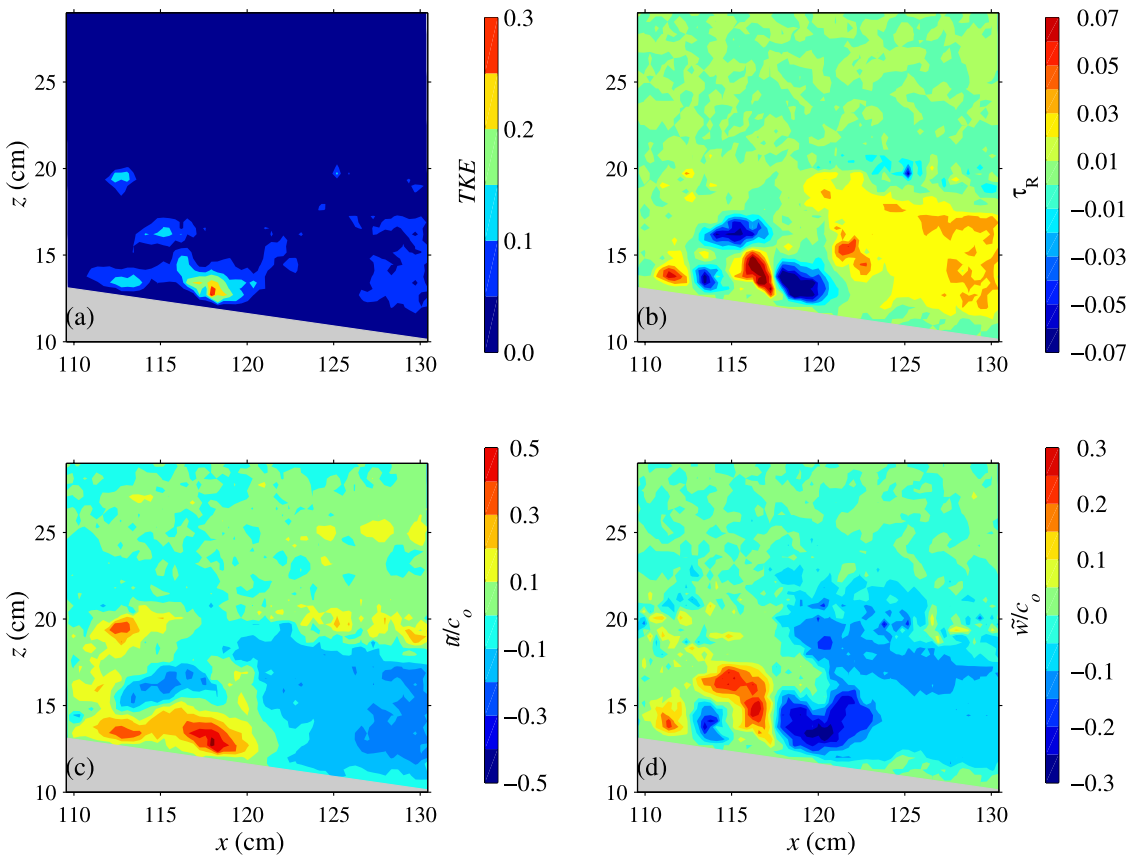

Figure 10. Instantaneous nondimensional (a) turbulent kinetic energy TKE = $(\tilde{u}^2 + \tilde{w}^2)/c_o^2$, (b) periodic Reynolds stress $\tau_R = \tilde{u}\tilde{w}/c_o^2$, (c) periodic horizontal velocity $\tilde{u}/c_o$, and (d) periodic vertical velocity $\tilde{w}/c_o$, during the resuspension event (i.e., Figures 5k, 6k, and 7k). Horizontal velocities are positive to the left (i.e., the upslope direction).

resuspension as a function of only τ_o and in particular U (see section 1); the positive near-bed τ_R must also be explicitly considered.

4. Discussion

4.1. Breaking Criterion and Mechanism

[39] To aid with the interpretation of field observations, which are at discrete intervals in both space and time, it is desirable to determine the location of wave breaking in terms of flow parameters that are external to the breaking process. Most studies to date have been concerned with wave breaking upon the slope-shelf topography typically characteristic to the coastal ocean [e.g., *Helfrich and Melville*, 1986; *Vlasenko and Hutter*, 2002]. The breaking criterion defined in these studies makes use of the fluid depth on the shelf; a parameter that is not defined in our closed slope geometry.

[40] Comparatively fewer studies have considered NLIW breaking at a topographic ridge. For this geometry *Sveen et al.* [2002] found breaking to occur when the fluid velocity in the lower layer exceeds 0.7 of a local nonlinear wave speed (c), defined at the top of the ridge. This parameter is also not defined for a closed slope.

[41] If we normalize the maximum horizontal velocity in the domain by the more easily computed linear wave speed (c_o), our results are similar to those of *Sveen et al.* [2002], and wave breaking (overturning) occurs with a maximum fluid velocity at the wave crest $|u|_{max} \approx 0.7c_o$ in the direction of wave propagation (Figure 12). In the lower layer $u \rightarrow c_o$ because of the drawdown beneath the shoaling wave; however, this velocity signature is unlikely a direct precursor to overturning as it is in the direction opposite to wave propagation and occurs a considerable time before wave overturning. Applying the nonlinear phase speed correction $c \approx 1.08c_o$ [*Boegman et al.*, 2003] overturning occurs when $u \approx 0.64c$. For closed slopes, the location of breaking can also be determined in terms of the undisturbed lower-layer depth at the breaking point and the distance from the beginning of the slope to the undisturbed interface/slope intersection. This criterion is given by *Helfrich* [1992] and *Boegman et al.* [2005b].

[42] *Carr and Davies* [2006] and *Diamessis and Redekopp* [2006] show the generation of a unsteady reversed flow boundary jet beneath large-amplitude NLIWs propagating over flat bottoms (i.e., jet flow in the same direction as the wave propagation but the opposite direction to the wave-induced lower-layer velocity). This jet is attributed to boundary layer separation in the adverse pressure gradient region of the wave-induced flow. For sufficiently large-amplitude waves relative to the lower-layer depth, global instability may occur where separation vortices are shed and ascend into the water column. For the case with a sloping bottom, we observe a near-bed upslope jet as a precursor to flow

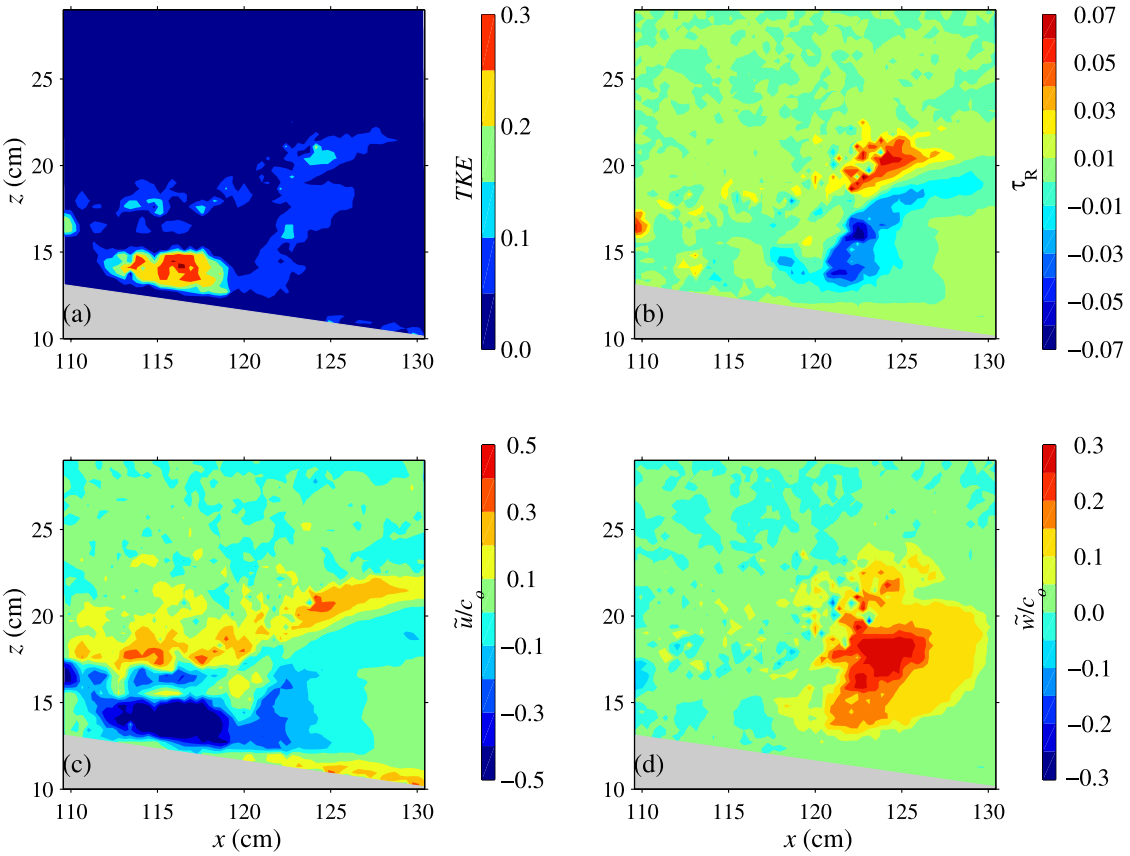

Figure 11. Instantaneous nondimensional (a) turbulent kinetic energy TKE = $(\tilde{u}^2 + \tilde{w}^2)/c_o^2$, (b) periodic Reynolds stress $\tau_R = \tilde{u}\tilde{w}/c_o^2$, (c) periodic horizontal velocity $\tilde{u}/c_o$, and (d) periodic vertical velocity $\tilde{w}/c_o$, during the drawdown (i.e., Figures 5e, 6i, 6j, 7i, and 7j). Horizontal velocities are positive to the left (i.e., the upslope direction).

separation beneath the shoaling NLIW (Figures 6i, 6j, 6k, 6l, 7i, 7j, 7k, and 7l). Because of the shoaling nature of our bottom bathymetry (i.e., variable h_2 along the slope), the critical wave amplitude requirement may be satisfied leading to global instability prior to convective breaking (P. Aghsaee, unpublished data, 2008); although this is not the case in the present set of observations. The upslope jet may also be enhanced because of the wave passing through the turning point (where $h_1 = h_2$), beyond which the rear face changes polarity from a wave of depression to a wave of elevation causing the flow beneath rear face to become characteristically in the same direction as the boundary jet (upslope).

4.2. Resuspension Mechanism

[43] We have presented laboratory observations of wave-induced resuspension that are physically consistent with turbulent channel flows [*Ikeda and Asaeda*, 1983; *Lapointe*, 1996; *Zelder and Street*, 2001; *Hosegood and van Haren*, 2004] and oceanic observations of breaking internal waves [*Hosegood and van Haren*, 2004], where the stress distributions are highly variable and sediment resuspension is strongly correlated to the vertical velocity component. These observations can be interpreted by analogy to the eddy-stress models of *Bagnold* [1966] and *Sutherland* [1967], where the underlying suspension mechanism is observationally consistent with these models, although those in the present study result from wave-coherent eddies that form in a transient flow separation process and not from coherent structures within a steady turbulent flow.

[44] More recently, observations of sediment resuspension in turbulent channel flows have been interpreted in terms of the turbulent bursting phenomenon. Here, we adopt the nomenclature of *Robinson* [1991], where a turbulent burst cycle consists of a sweep of high-speed fluid inward toward the wall and an ejection of low-speed fluid outward from the wall. Laboratory experiments in channels with smooth or rippled beds show transport of sediment associated with a net upward momentum flux in the outer region of the boundary layer and a net downward momentum flux closer to the wall [*Sumer and Deigaard*, 1981; *Wei and Willmarth*, 1991]. It was suggested that these fluxes were turbulent ejections and sweeps, respectively, as found in a classical turbulent boundary layer. These bursting models have also been applied to field observations. *Gordon* [1975] interpreted intermittent periods of high-momentum transport in tidal boundary layers as bursts and sweeps. *Soulsby et al.* [1994] found resuspension in an estuary boundary layer to be strongly correlated to ejections and clearer water was weakly correlated to sweeps. *Lapointe* [1996] traced 20–90% of the net resuspension in a sand-bed river to energetic burst-like turbulent events during which upward transport of momentum and sediment are correlated. More recently, *Bonnin et al.* [2006] attributed resuspension at the foot of the continental slope (3000 m depth) to bursts in

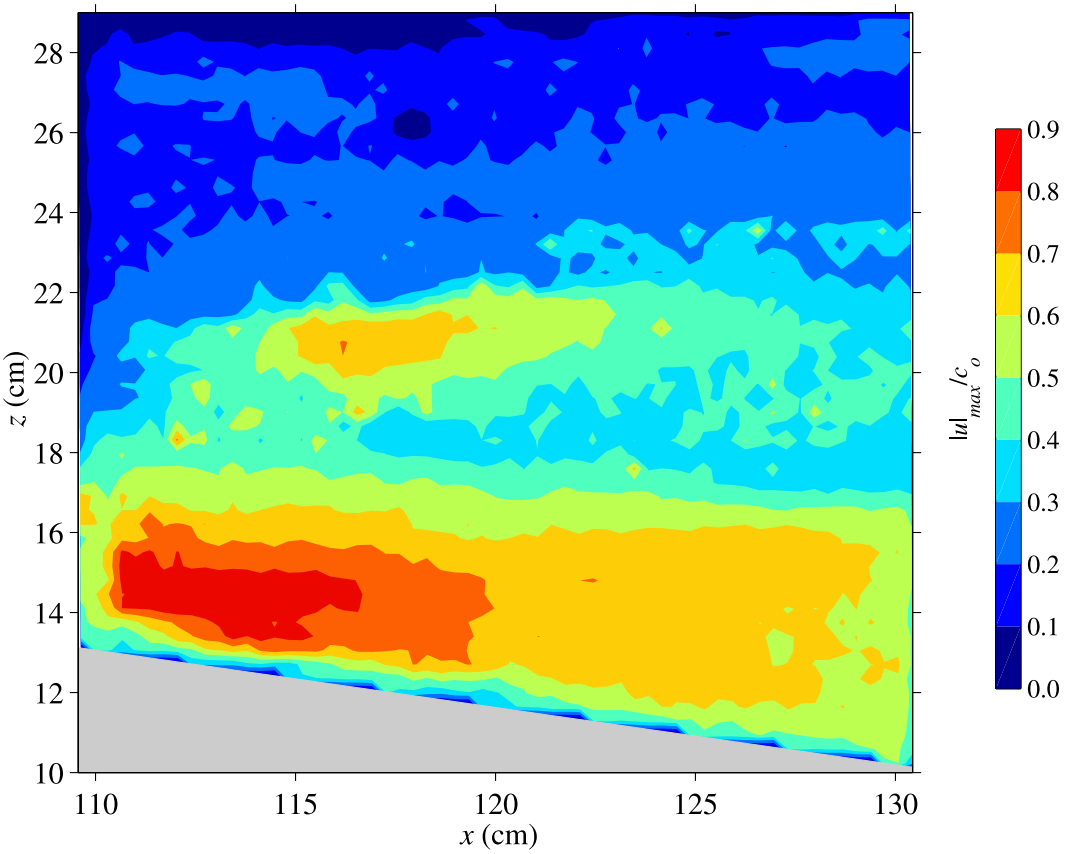

Figure 12. Absolute value of the maximum horizontal velocity observed during the wave-breaking event. The velocity is nondimensionalized by $c_o = \sqrt{g' h_1 h_2 / H} \approx 0.11$ m s^{-2}.

velocity; possibly energized by gravity currents. The presence of large-scale topography will cause a localized intensification in sweeps, ejections, resuspension and flow separation [*Jackson*, 1976; *Bennett and Best*, 1995]. By correlating ejections and sweeps with the positive and negative τ_R events, respectively, it is natural to extend the bursting model to our observations of NLIW shoaling over sloping topography.

[45] The similarities between observations of wave-induced vortex resuspension and resuspension due to eddy-stress and turbulent bursting may be reconciled by noting that most conceptualizations of the bursting process describe the passage of one or more tilted, quasi-streamwise vortices which eject low-speed fluid away from the wall by vortex induction [*Robinson*, 1991]. This conceptualization is analogous to the eddy-stress model put forward by *Sutherland* [1967] (Figure 13); thus suggesting a unified resuspension model for geophysical resuspension events driven by vortical or eddy-like structures that impinge upon the sediment boundary.

4.3. Generalization to Field Scale

[46] Resuspension beneath shoaling surface waves has been investigated thoroughly at the field scale and it is instructive to discuss how our laboratory results compare to these studies. Barotropic wavy flows in the absence of a free-stream component (e.g., wave groups in the surf zone) are typically decomposed by band-passing the signal in the inertial subrange, as defined by spectral slope breaks, such that Reynolds stresses are obtained [e.g., *Smyth and Hay*, 2003; *Kularatne and Pattiaratchi*, 2008]. Resuspension has been correlated with coherent structures beneath the shoaling waves and high-concentration eddies, greater that 2 to 5 times the thickness of the wave boundary layer have been observed and are postulated to be either wave-coherent eddies associated with shoaling (as observed herein) or random coherent structures within the turbulent flow (inertial subrange) that occur at the higher Reynolds numbers associated with field-scale barotropic flows [*Hay and Bowen*, 1994]. High suspended sediment concentrations were related

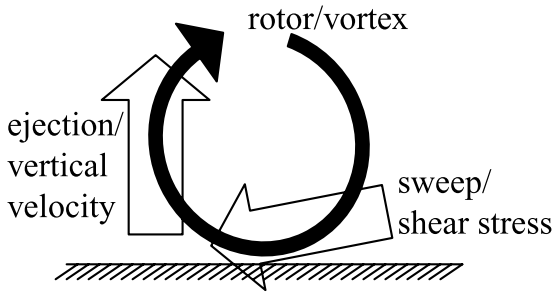

Figure 13. Schematic showing the similarities between the eddy-stress and turbulent bursting resuspension mechanisms.

to burst events in the Reynolds stress [*Kularatne and Pattiaratchi*, 2008].

[47] Despite these similarities, it is difficult to directly compare barotropic field and baroclinic laboratory results. Inertial band-passing of field data may remove the signal associated with the wave-coherent eddies, as these are the energy containing eddies occurring at low frequency. In the present study, it is these wave-coherent eddies that directly lead to resuspension. Moreover, inertial-type turbulence is not observed to occur until well after resuspension and wave breaking (Figures 6w and 6x). These differences in processing (spectral filtering vs. time averaging) and frequencies related to resuspension (inertial versus subinertial components) make direct comparisons difficult. Both high-*Re* laboratory experiments and high spatial resolution field observations are required.

[48] As is common in laboratory studies, we have exaggerated the vertical scale relative to the horizontal to mitigate boundary effects. Studies at the laboratory scale will also have a reduced wave Reynolds number $Re_w \sim c_o a/\nu$ relative to the field. To investigate if the exaggerated vertical scale is causing an exaggerated vertical velocity, which puts bias in the resuspension mechanism, we compare our results at $Re_w \sim 10^3$ to those achieved by others. In other laboratory studies Re_w is of the same order ($\sim 10^3$). *Sveen et al.* [2002] define a breaking criterion in terms of the horizontal velocity but do not mention the vertical velocity component in the breaking region; however, they note that during vigorous breaking events particles are transported vertically across the layer interface. *Carr and Davies* [2006] note that above the bottom boundary there are short intervals in which relatively strong vertical motions are observed. Vertical velocities are an order of magnitude less than horizontal velocities (as shown in Figure 9). Two-dimensional numerical results at slightly larger scale, $Re_w \sim 10^4$, by *Diamessis and Redekopp* [2006] are similar to those by *Carr and Davies* [2006]; except that the separation bubbles tend to be smaller and more numerous, clustering in groups with similar effects as larger bubbles at smaller Re_w on wave breaking (P. Aghsaee, unpublished data, 2008). In lakes and the ocean $Re_w \sim 10^6$ and 10^7, respectively [e.g., *Farmer and Smith*, 1978; *Sandstrom and Elliott*, 1984; *Stanton and Ostrovsky*, 1998; *Boegman et al.*, 2003], and the vertical to horizontal aspect ratio is not distorted. In both this study and in oceanic field observations [*Caldwell and Chriss*, 1979], the thickness of the viscous sublayer is estimated to be $\sim$1 mm. The oceanic observations by *Hosegood and van Haren* [2004] are also analogous to the laboratory observations presented herein, with similar nondimensional vortex diameters and strong vertical velocities that correlate to massively enhanced sediment fluxes. The effects of Re_w on other processes such as mixing efficiency and dissipation also remain unknown and require further study.

[49] Laboratory experiments [*Boegman et al.*, 2005b] show that at lab scale, the plunging/convective breaker observed in the present experiments should only occur over a limited range of geophysical parameters in the field (range of wave slopes a/λ and bed slopes, s) as determined by an internal form of the Iribarren number $\xi = s/(a/\lambda)^{1/2}$. For much larger and smaller ξ, the breaking mechanism (as shown herein) may be suppressed by buoyancy and viscosity, respectively, or the wave may degenerate via fission or global instability.

5. Conclusions

[50] Laboratory experiments of shoaling NLIWs on closed slopes were undertaken revealing a breaking mechanism that is dynamically consistent with the conceptual rotor model proposed by *Thorpe* [1998]. The rotor is observed to result from flow separation within the adverse pressure gradient region beneath the shoaling wave. The rotor initiates sediment motion through enhanced negative Reynolds stress as it impinges upon the viscous sublayer and then vertically entrains the sediment through local positive Reynolds stress resulting from a strong vertical component of the wave-coherent velocity. The locations of resuspension are also consistent with regions where the mean (wave-averaged) vertical velocity is directed outward from the wall. Elevated levels of near-bed turbulent kinetic energy were observed that were not correlated to the resuspension events.

[51] These observations are in agreement with the limited field measurements of resuspension beneath shoaling NLIWs [*Hosegood and van Haren*, 2004]. The results demonstrate that it is not sufficient to model resuspension as a function of the near-bed viscous stress alone and models that employ this parameter, and neglect the dynamics of near-bed turbulence, are inappropriate for modeling resuspension because of NLIW shoaling. This result is not unexpected since the turbulent BBL is nonstationary. The Reynolds stress component of the near-bed flow must be explicitly considered when modeling resuspension.

[52] **Acknowledgments.** Kevin Lamb and Peter Diamessis are thanked for discussions on internal waves, as is J. Kristian Sveen for help with MatPIV. We also thank the anonymous reviewers for their comments and directing us to *Cantwell and Coles'* [1983] paper. The experiments were conducted while L.B. was a postdoctoral fellow at the University of Western Australia, funded by the Australian Research Council. A draft of the paper was written while L.B. was at Scripps Institution of Oceanography under the support of an Office of Naval Research grant to Kraig Winters.

References

Bagnold, R. A. (1966), An approach to the sediment transport problem from general physics, *U.S. Geol. Surv. Prof. Paper, 422–I*.

Bennett, S. J., and J. L. Best (1995), Mean flow and turbulence structure over fixed two-dimensional dunes: Implications for sediment transport and bedform stability, *Sedimentology*, *42*, 491–513.

Boegman, L., J. Imberger, G. N. Ivey, and J. P. Antenucci (2003), High-frequency internal waves in large stratified lakes, *Limnol. Oceanogr.*, *48*, 895–919.

Boegman, L., G. N. Ivey, and J. Imberger (2005a), The energetics of large-scale internal wave degeneration in lakes, *J. Fluid Mech.*, *531*, 159–180.

Boegman, L., G. N. Ivey, and J. Imberger (2005b), The degeneration of internal waves in lakes with sloping topography, *Limnol. Oceanogr.*, *50*, 1620–1637.

Bogucki, D., T. Dickey, and L. G. Redekopp (1997), Sediment resuspension and mixing by resonantly generated internal solitary waves, *J. Phys. Oceanogr.*, *27*, 1181–1196.

Bogucki, D. J., L. G. Redekopp, and J. Barth (2005), Internal solitary waves in the Coastal Mixing and Optics 1996 experiment: Multimodal structures and resuspension, *J. Geophys. Res.*, *110*, C02024, doi:10.1029/2003JC002253.

Bonnin, J., H. van Haren, P. Hosegood, and G.-J. A. Brummer (2006), Burst resuspension of seabed material at the foot of the continental slope in the Rockall Channel, *Mar. Geol.*, *226*, 167–184.

Cacchione, D. A., and D. Drake (1986), Nepheloid layers and internal waves over continental shelves and slopes, *Geo Mar. Lett.*, *6*, 147–152.

Caldwell, D. R., and T. M. Chriss (1979), The viscous sublayer at the sea floor, *Science*, *205*, 1131–1132.

Cantwell, B., and D. Coles (1983), An experimental study of entrainment and transport in the turbulent near wake of a circular cylinder, *J. Fluid Mech.*, *136*, 321–374.

Carr, M., and P. A. Davies (2006), The motion of an internal solitary wave of depression over a fixed bottom boundary in a shallow, two-layer fluid, *Phys. Fluids*, *18*, 16,601, doi:10.1063/1.2162033.

Diamessis, P. J., and L. G. Redekopp (2006), Numerical investigation of solitary internal wave-induced global instability in shallow water benthic boundary layers, *J. Phys. Oceanogr.*, *36*, 784–812.

Dickey, T. D., G. C. Chang, Y. C. Agrawal, A. Williams III, and P. S. Hill (1998), Sediment resuspension in the wakes of Hurricanes Edouard and Hortense, *Geophys. Res. Lett.*, *25*, 3533–3536.

Drake, D. E., and D. A. Cacchione (1986), Field observations of bed shear stress and sediment resuspension on continental shelves, Alaska and California, *Cont. Shelf Res.*, *6*, 415–429.

Farmer, D., and J. D. Smith (1978), Nonlinear internal waves in a fjord, in *Hydrodynamics of Estuaries and Fjords*, edited by J. C. J. Nihoul, *Elsevier Oceanogr. Ser.*, vol. 23, pp. 465–493.

Foster, D. L., R. A. Beach, and R. A. Holman (2006), Turbulence observations of the nearshore wave bottom boundary layer, *J. Geophys. Res.*, *111*, C04011, doi:10.1029/2004JC002838.

Gordon, C. M. (1975), Period between bursts at high Reynolds number, *Phys. Fluids*, *18*, 141–143.

Hammond, D. A., and L. G. Redekopp (1998), Local and global instability properties of separation bubbles, *Eur. J. Mech., Part B: Fluids*, *17*, 145–164.

Hawley, N. (2004), Response of the benthic nepheloid layer to near-inertial internal waves in southern Lake Michigan, *J. Geophys. Res.*, *109*, C04007, doi:10.1029/2003JC002128.

Hay, A. E., and A. J. Bowen (1994), Coherence scales of wave-induced suspended sand concentration fluctuations, *J. Geophys. Res.*, *99*, 12,749–12,765.

Helfrich, K. R. (1992), Internal solitary wave breaking and run-up on a uniform slope, *J. Fluid Mech.*, *243*, 133–154.

Helfrich, K. R., and W. K. Melville (1986), On nonlinear internal waves over slope-shelf topography, *J. Fluid Mech.*, *167*, 285–308.

Horn, D. A., J. Imberger, and G. N. Ivey (2001), The degeneration of large-scale interfacial gravity waves in lakes, *J. Fluid Mech.*, *434*, 181–207.

Hosegood, P., and H. van Haren (2004), Near-bed solibores over the continental slope in the Faeroe-Shetland Channel, *Deep Sea Res., Part II*, *51*, 2943–2971, doi:10.1016/j.dsr.2004.09.016.

Ikeda, S., and T. Asaeda (1983), Sediment suspension with rippled bed, *J. Hydraul. Eng.*, *109*, 409–423.

Jackson, C. (2007), Internal wave detection using the Moderate Resolution Imaging Spectroradiometer (MODIS), *J. Geophys. Res.*, *112*, C11012, doi:10.1029/2007JC004220.

Jackson, R. G. (1976), Sedimentological and fluid-dynamic implications of the bursting turbulent phenomenon in geophysical flows, *J. Fluid Mech.*, *77*, 531–560.

Kao, T. W., F. S. Pan, and D. Renouard (1985), Internal solitons on the pycnocline generation, propagation, shoaling and breaking over a slope, *J. Fluid Mech.*, *159*, 19–53.

Klymak, J. M., and J. N. Moum (2003), Internal solitary waves of elevation advancing on a shoaling shelf, *Geophys. Res. Lett.*, *30*(20), 2045, doi:10.1029/2003GL017706.

Kuhrts, C., W. Fennel, and T. Seifert (2004), Model studies of transport of sedimentary material in the western Baltic, *J. Mar. Syst.*, *52*, 167–190, doi:10.1016/j.jmarsys.2004.03.005.

Kularatne, S. R., and C. Pattiaratchi (2008), Turbulent kinetic energy and sediment resuspension due to wave groups, *Cont. Shelf Res.*, *28*, 726–736, doi:10.1016/j.csr.2007.12.007.

Lamb, K. G. (2003), Shoaling solitary internal waves: On a criterion for the formation of waves with trapped cores, *J. Fluid Mech.*, *479*, 81–100.

Lapointe, M. F. (1996), Frequency spectra and intermittency of the turbulent suspension process in a sand-bed river, *Sedimentology*, *43*, 439–449.

Lorke, A., L. Umlauf, T. Jonas, and A. Wüest (2002), Dynamics of turbulence in low-speed oscillating bottom-boundary layers of stratified basins, *Environ. Fluid Mech.*, *2*, 291–313.

MacIntyre, S., K. M. Flynn, R. Jellison, and J. R. Romero (1999), Boundary mixing and nutrient fluxes in Mono Lake, California, *Limnol. Oceanogr.*, *4*, 512–529.

McPhee-Shaw, E. E., R. Sternbergb, B. Mullenbachc, and A. Ogston (2004), Observations of intermediate nepheloid layers on the northern California continental margin, *Cont. Shelf Res.*, *24*, 693–720, doi:10.1016/j.csr.2004.01.004.

Michallet, H., and G. N. Ivey (1999), Experiments on mixing due to internal solitary waves breaking on uniform slopes, *J. Geophys. Res.*, *104*, 13,467–13,477.

Puig, P., A. Palanques, J. Guillén, and M. El Khatab (2004), Role of internal waves in the generation of nepheloid layers on the northwestern Alboran slope: Implications for continental margin shaping, *J. Geophys. Res.*, *109*, C09011, doi:10.1029/2004JC002394.

Reynolds, W. C., and A. K. M. F. Hussain (1972), The mechanics of an organized wave in turbulent shear flow. Part 3. Theoretical models and comparison with experiments, *J. Fluid Mech.*, *54*, 263–288.

Ribbe, J., and P. E. Holloway (2001), A model of suspended sediment transport by internal tides, *Cont. Shelf Res.*, *21*, 395–422.

Robinson, S. K. (1991), Coherent motions in the turbulent boundary layer, *Annu. Rev. Fluid Mech.*, *23*, 601–639, doi:10.1146/annurev.fl.23.010191.003125.

Sandstrom, H., and J. A. Elliott (1984), Internal tide and solitons on the Scotian Shelf: A nutrient pump at work, *J. Geophys. Res.*, *89*, 6415–6426.

Smyth, C., and A. E. Hay (2003), Near-bed turbulence and bottom friction during SandyDuck97, *J. Geophys. Res.*, *108*(C6), 3197, doi:10.1029/2001JC000952.

Soulsby, R. L., R. Atkins, and A. P. Salkield (1994), Observations of the turbulent structure of a suspension of sand in a tidal current, *Cont. Shelf Res.*, *14*, 429–435.

Stacey, M. T., S. G. Monismith, and J. R. Burau (1999), Measurements of Reynolds stress profiles in unstratified tidal flow, *J. Geophys. Res.*, *104*, 10,933–10,949.

Stanton, T. P., and L. A. Ostrovsky (1998), Observations of highly nonlinear internal solitons over the Continental Shelf, *Geophys. Res. Lett.*, *25*, 2695–2698.

Stastna, M., and K. G. Lamb (2002), Vortex shedding and sediment resuspension associated with the interaction of an internal solitary wave and the bottom boundary layer, *Geophys. Res. Lett.*, *29*(11), 1512, doi:10.1029/2001GL014070.

Sumer, B. M., and R. Deigaard (1981), Particle motions near the bottom in turbulent flow in an open channel. Part 2, *J. Fluid Mech.*, *109*, 311–337.

Sutherland, A. J. (1967), Proposed mechanism for sediment entrainment by turbulent flows, *J. Geophys. Res.*, *72*, 6183–6194.

Sveen, J. K. (2004), An introduction to MatPIV v.1.6.1, *Eprint 2*, Dep. of Math., Univ. of Oslo, Oslo (http://www.math.uio.no/~jks/matpiv).

Sveen, J. K., Y. Guo, P. A. Davies, and J. Grue (2002), On the breaking of internal solitary waves at a ridge, *J. Fluid Mech.*, *469*, 161–188.

Thorpe, S. A. (1998), Some dynamical effects of internal waves and the sloping sides of lakes, in *Physical Processes in Lakes and Oceans*, *Coastal Estaurine Stud.*, vol. 54, edited by J. Imberger, pp. 441–460, AGU, Washington, D. C.

Venayagamoorthy, S. K., and O. B. Fringer (2007), On the formation and propagation of nonlinear internal boluses across a shelf break, *J. Fluid Mech.*, *577*, 137–159.

Veron, F., G. Saxen, and S. K. Misra (2007), Measurements of the viscous tangential stress in the airflow above wind waves, *Geophys. Res. Lett.*, *34*, L19603, doi:10.1029/2007GL031242.

Vlasenko, V., and K. Hutter (2002), Numerical experiments on the breaking of solitary internal waves over a slope-shelf topography, *J. Phys. Oceanogr.*, *32*, 1779–1793.

Wallace, B. C., and D. L. Wilkinson (1988), Run-up of internal waves on a gentle slope in a two-layered system, *J. Fluid Mech.*, *191*, 419–442.

Wang, X. H., and N. Pinardi (2002), Modeling the dynamics of sediment transport and resuspension in the northern Adriatic Sea, *J. Geophys. Res.*, *107*(C12), 3225, doi:10.1029/2001JC001303.

Webster, D. R., P. J. W. Roberts, and L. Ra'ad (2001), Simultaneous DPTV/PLIF measurements of a turbulent jet, *Exp. Fluids*, *30*, 65–72.

Wei, T., and W. W. Willmarth (1991), Examination of *v*-velocity fluctuations in a turbulent channel flow in the context of sediment transport, *J. Fluid Mech.*, *223*, 241–252.

Wessels, F., and K. Hutter (1996), Interaction of internal waves with a topographic sill in a two-layered fluid, *J. Phys. Oceanogr.*, *26*, 5–20.

Wiberg, P. L., D. E. Drake, and D. A. Cacchione (1994), Sediment resuspension and bed armoring during high bottom stress events on the northern California inner continental shelf: Measurements and prediction, *Cont. Shelf Res.*, *14*, 1191–1219.

Winters, K. B., H. E. Seim, and T. D. Finnigan (2000), Simulation of nonhydrostatic, density-stratified flow in irregular domains, *Int. J. Numer. Methods Fluids*, *32*, 263–284.

Zelder, E. A., and R. L. Street (2001), Large-eddy simulation of sediment transport: Currents over ripples, *J. Hydraul. Eng.*, *127*, 444–452.

L. Boegman, Department of Civil Engineering, Queen's University, Kingston, ON K7L3N6, Canada. (www.civil.queensu.ca/people/faculty/boegman/)

G. N. Ivey, School of Environmental Systems Engineering, University of Western Australia, Crawley, WA 6009, Australia.